


Chern Fermi pocket, topological pair density wave, and charge-4e and charge-6e superconductivity in kagomé superconductors

Received: 15 March 2022

Sen Zhou^{1,2}  & Ziqiang Wang³ 

Accepted: 1 November 2022

Published online: 26 November 2022

 Check for updates

The recent discovery of novel charge density wave (CDW) and pair density wave (PDW) in kagomé lattice superconductors AV_3Sb_5 ($A = K, Rb, Cs$) hints at unexpected time-reversal symmetry breaking correlated and topological states whose physical origin and broader implications are not understood. Here, we make conceptual advances toward a mechanism behind the striking observations and new predictions for novel macroscopic phase coherent quantum states. We show that the metallic CDW state with circulating loop currents is a doped orbital Chern insulator near van Hove filling. The emergent Chern Fermi pockets (CFPs) carry concentrated Berry curvature and orbital magnetic moment. We find that the pairing of electrons on the CFPs leads to a superconducting state with an emergent vortex-antivortex lattice and the formation of a complex triple-**Q** PDW. A plethora of correlated and topological states emerge, including a never-before-encountered chiral topological PDW superconductor, a loop-current pseudogap phase, and vestigial charge-4e and charge-6e superconductivity in staged melting of the vortex-antivortex lattice and hexatic liquid crystal. Our findings reveal previously unknown nature of the superconducting state of a current-carrying Chern metal, with broad implications for correlated and topological materials.

The field of transition-metal kagomé lattice materials has leapt forward with the discovery of superconductivity in a new family of vanadium-based kagomé metals AV_3Sb_5 ($A = K, Rb, Cs$)^{1,2}. In contrast to the insulating kagomé compounds extensively studied for quantum spin liquids and doped Mott insulators^{3–5}, AV_3Sb_5 are nonmagnetic correlated metals with itinerant electrons traversing the geometrically frustrated kagomé lattice. They are complementary to the (Fe, Co, Mn)-based itinerant kagomé magnets that exhibit rich correlated topological phenomena^{6–11}, but have remained nonsuperconducting at low temperatures.

All AV_3Sb_5 undergo charge density wave (CDW) transitions below $T_{cdw} \sim 78 - 103$ K and superconducting (SC) transitions below $T_c \sim 0.9 - 2.5$ K. Both diagonal and off-diagonal long-range ordered states turn out to be highly intriguing and display a complex landscape of

spontaneous symmetry breaking phases. The CDW state has $2a_0 \times 2a_0$ charge order in the kagomé plane stacked along the *c*-axis^{12–19}. Despite the absence of magnetism, the CDW state shows evidence of spontaneous time-reversal symmetry (TRS) breaking^{12,20–22} and exhibits giant anomalous Hall effect (AHE)^{23,24}. The CDW state also breaks rotation symmetry^{12,13,15,19,25}. Below T_c , a pair density wave (PDW) order was discovered¹⁵, where the finite-momentum pairing modulates the SC gap and coherence peaks with $\frac{4}{3}a_0 \times \frac{4}{3}a_0$ periodicity. The primary PDW produces an unexpected pseudogap phase in striking comparison to the high- T_c cuprates¹⁵.

The physical origin and implication of these remarkable observations are currently unknown. We study them here in order to understand quantum materials exhibiting both the intrinsic AHE and superconductivity. We show that, close to the van Hove (vH) filling, the

¹CAS Key Laboratory of Theoretical Physics, Institute of Theoretical Physics, Chinese Academy of Sciences, 100190 Beijing, China. ²School of Physical Sciences & CAS Center for Excellence in Topological Quantum Computation, University of Chinese Academy of Sciences, 100049 Beijing, China.

³Department of Physics, Boston College, Chestnut Hill, MA 02467, USA. ✉ e-mail: zhousen@itp.ac.cn; wangzi@bc.edu

breathing kagomé lattice with circulating current gives rise to a loop-current Chern metal with Chern Fermi pockets (CFPs) carrying concentrated Berry curvature, which can account for the observed quantum oscillations^{18,26,27} and the large intrinsic AHE^{23,24}. The SC state arising from the normal state Chern metal with loop currents turns out to be highly unconventional, since the supercurrents must circulate around spontaneously nucleated vortices. We find that finite momentum pairing on the CFPs leads to novel roton PDW states with an emergent vortex-antivortex lattice. Remarkably, due to the Fermi surface (FS) reconstruction in the $2a_0 \times 2a_0$ CDW state, the CFPs are connected by the wavevector $\frac{3}{4}\mathbf{Q}_{\text{Bragg}}$, leading to the triple- \mathbf{Q} roton PDW with the observed $\frac{4}{3}a_0 \times \frac{4}{3}a_0$ periodicity¹⁵.

Superconductivity intertwined with broken spatial symmetries generates a landscape of extraordinary correlated and topological states that are relevant for current experiments. We find a fully gapped chiral topological PDW superconductor protected by an induced uniform charge- $2e$ condensate. The phases that straddle the SC ground state and the normal state Chern metal are intriguing. Staged melting of the vortex-antivortex lattice and hexatic liquid crystal state by the proliferation of topological defects such as dislocations and disclinations produces spatially uniform charge- $4e$ superconductivity with orientational order and isotropic charge- $6e$ superconductivity. Alternatively, destroying the SC phase coherence before restoring the crystalline symmetry leads to a loop-current pseudogap phase.

Results

Breathing kagomé lattice

In the AV_3Sb_5 compounds, V atoms form an ideal kagomé lattice coordinated by Sb atoms and the alkali atoms (A) intercalate between the kagomé layers. Very similar band structures are predicted across the series by the density functional theory (DFT)^{1,16}, in overall agreement with the measured band dispersions^{2,28–32}. There is an electron FS around the center of the hexagonal Brillouin zone (BZ) derived from the Sb p_z orbital, while the actions of the low-energy V d -orbitals are located near the zone boundary, forming quasi-2D FS sheets close to the vH singularities.

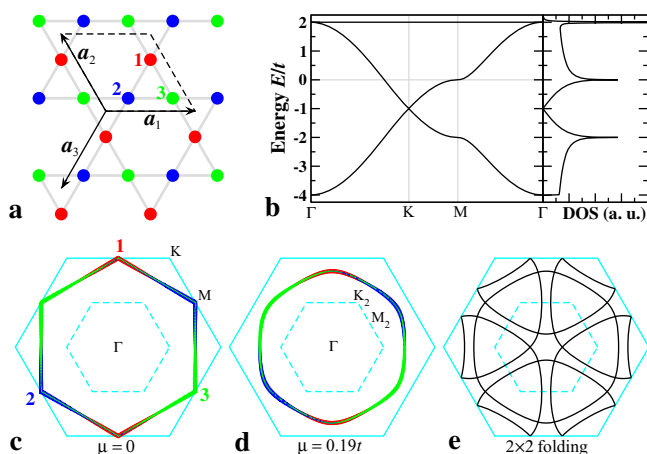


Fig. 1 | Itinerant fermions on kagomé lattice. **a** Lattice structure with three sublattices denoted by red (1), blue (2), and green (3) circles. The two basis vectors defining the unit cell are $\mathbf{a}_1 = (1, 0)$ and $\mathbf{a}_2 = (-\frac{1}{2}, \frac{\sqrt{3}}{2})$. The reciprocal lattice vectors $\mathbf{b}_1 = \frac{4\pi}{\sqrt{3}}(\frac{\sqrt{3}}{2}, \frac{1}{2})$ and $\mathbf{b}_2 = \frac{4\pi}{\sqrt{3}}(0, -1)$. The third direction follows $\mathbf{a}_3 = -\mathbf{a}_1 - \mathbf{a}_2$ and $\mathbf{b}_3 = -\mathbf{b}_1 - \mathbf{b}_2$. **b** Band dispersion and DOS. Fermi level at vH filling is marked by the grey line at $\mu = 0$. **c** FS at vH filling in the hexagonal BZ (solid cyan curves). Thickness of colored lines and numbers display the sublattice contents. The high symmetry points $\Gamma = (0, 0)$, $K = (\pm\frac{2\pi}{3}, 0)$, $M = (0, \pm\frac{2\pi}{3})$, and $M_2 = (\pm\pi, \pm\frac{\pi}{\sqrt{3}})$. **d** Sublattice resolved FS at $\mu = 0.19t$ for electron doping above vH filling. Dashed cyan curves enclose the 2×2 reduced BZ with the resulting high symmetry points denoted by $K_2 = \frac{1}{2}K$ and $M_2 = \frac{1}{2}M$. **e** FS in (d) folded by the 2×2 BZ boundary.

To capture the most essential physics of a d band crossing the Fermi level near the vH point, we consider the one-orbital model on the kagomé lattice as depicted in Fig. 1a with the lattice constant $a_0 \equiv 1$. The locations of the three sublattices in the unit cell at \mathbf{r} are given by $\mathbf{r}_1 = \mathbf{r} - \frac{1}{2}\mathbf{a}_3$, $\mathbf{r}_2 = \mathbf{r}$, and $\mathbf{r}_3 = \mathbf{r} + \frac{1}{2}\mathbf{a}_1$. The tight-binding model for the corner-sharing up and down triangles of the kagomé lattice is written as,

$$H_{\text{tb}} = - \sum_{(\alpha\beta\gamma)\mathbf{r}} \left[t_{\alpha\beta}^u(\mathbf{r})c_{\alpha\mathbf{r}}^\dagger c_{\beta\mathbf{r}} + t_{\alpha\beta}^d(\mathbf{r})c_{\alpha\mathbf{r}}^\dagger c_{\beta\mathbf{r}-\mathbf{a}_\gamma} + h.c. \right] - \mu \hat{n}_{\alpha\mathbf{r}}, \quad (1)$$

where $c_{\alpha\mathbf{r}}^\dagger$ creates an electron on sublattice α in unit cell \mathbf{r} , $t_{\alpha\beta}^{u,d}(\mathbf{r})$ is the nearest-neighbor (nn) hopping in the up and down triangles between sublattices α and β , μ is the chemical potential, and $\hat{n}_{\alpha\mathbf{r}} = c_{\alpha\mathbf{r}}^\dagger c_{\alpha\mathbf{r}}$ is the density operator. The sublattice indices run over $(\alpha, \beta, \gamma) = (1, 2, 3), (2, 3, 1), (3, 1, 2)$ and spin indices are left implicit.

To reveal the unique geometry of the kagomé lattice, which plays a crucial role in the charge ordered state, we rewrite

$$H_{\text{tb}} = - \sum_{(\alpha\beta\gamma)\mathbf{r}} \left[t_{\alpha\beta}^+(\mathbf{r})\chi_{\alpha\beta}^+(\mathbf{r}) + t_{\alpha\beta}^-(\mathbf{r})\chi_{\alpha\beta}^-(\mathbf{r}) + h.c. \right] - \mu \hat{n}_{\alpha\mathbf{r}}, \quad (2)$$

where $t_{\alpha\beta}^\pm = \frac{1}{2}(t_{\alpha\beta}^u \pm t_{\alpha\beta}^d)$ and the corresponding symmetric (+) and antisymmetric (−) nn bond operators,

$$\chi_{\alpha\beta}^\pm(\mathbf{r}) = c_{\alpha\mathbf{r}}^\dagger c_{\beta\mathbf{r}} \pm c_{\alpha\mathbf{r}}^\dagger c_{\beta\mathbf{r}-\mathbf{a}_\gamma}. \quad (3)$$

For a kagomé lattice with uniform nn hopping, $t_{\alpha\beta}^+(\mathbf{r}) = t$ and $t_{\alpha\beta}^-(\mathbf{r}) = 0$. The corresponding band dispersion and density of states (DOS) are shown in Fig. 1b. A uniform $t_{\alpha\beta}^-(\mathbf{r}) = \delta \neq 0$ produces an intra-cell breathing kagomé lattice³³ without breaking lattice translation symmetry. A spatially modulated hopping $t_{\alpha\beta}^-(\mathbf{r}) = \delta \cos(\mathbf{Q} \cdot \mathbf{r})$ describes a breathing kagomé lattice with broken translation symmetry and a bond ordered CDW with wavevector \mathbf{Q} .

Complex CDW and Chern Fermi pockets

At band filling $n_{\text{vH}} = 5/12$ or $\mu = 0$, the sublattice-resolved FS is the hexagon connecting the vH singularity at the M points of the BZ in Fig. 1c. Theoretical studies at this vH filling have demonstrated a rich set of instabilities toward correlated states due to the unique sublattice quantum interference effects^{34–36}. The extended Coulomb interactions V can play a more important role than the local Hubbard U and produce a $2a_0 \times 2a_0$ bond ordered CDW, which is indeed consistent with the triple- \mathbf{Q} CDW observed in the multi-orbital AV_3Sb_5 where the Fermi level lies close to the d -bands vH singularities. The DFT calculations¹⁶ show that the $2a_0 \times 2a_0$ CDW is accompanied by the softening of the phonon breathing mode at the zone boundary M points of the kagomé lattice (Fig. 1c). This corresponds to the triple- \mathbf{Q} breathing modulation of the antisymmetric bond in Eq. (2) and is described by the Hamiltonian

$$H_{\text{cdw}} = \sum_{(\alpha\beta\gamma)\mathbf{r}} \rho_\gamma \cos(\mathbf{Q}_\gamma \cdot \mathbf{r}) \chi_{\alpha\beta}^-(\mathbf{r}) + h.c., \quad (4)$$

where the CDW wavevector $\mathbf{Q}_\gamma = \frac{1}{2}\mathbf{G}^\gamma$, with the Bragg vector $\mathbf{G}^{1,2,3} \equiv \mathbf{b}_{2,1,3}$. The CDW maintains rotation and inversion symmetry, and exhibits the star-of-David (SD) and inverse-SD (tri-hexagonal) bond configurations for $\rho_\gamma > 0$ and $\rho_\gamma < 0$, respectively. Nevertheless, these bond ordered CDWs are real and do not break TRS.

Motivated by the conjecture of spontaneous TRS breaking orbital currents¹², a long-sought after quantum state also relevant for the pseudogap phase in the high- T_c cuprates^{37–39} and the quantum anomalous Hall insulators⁴⁰, several theoretical studies have explored complex bond ordered triple- \mathbf{Q} CDWs supporting circulating current and plaquette flux^{41–44}. At the vH filling, the electron-electron

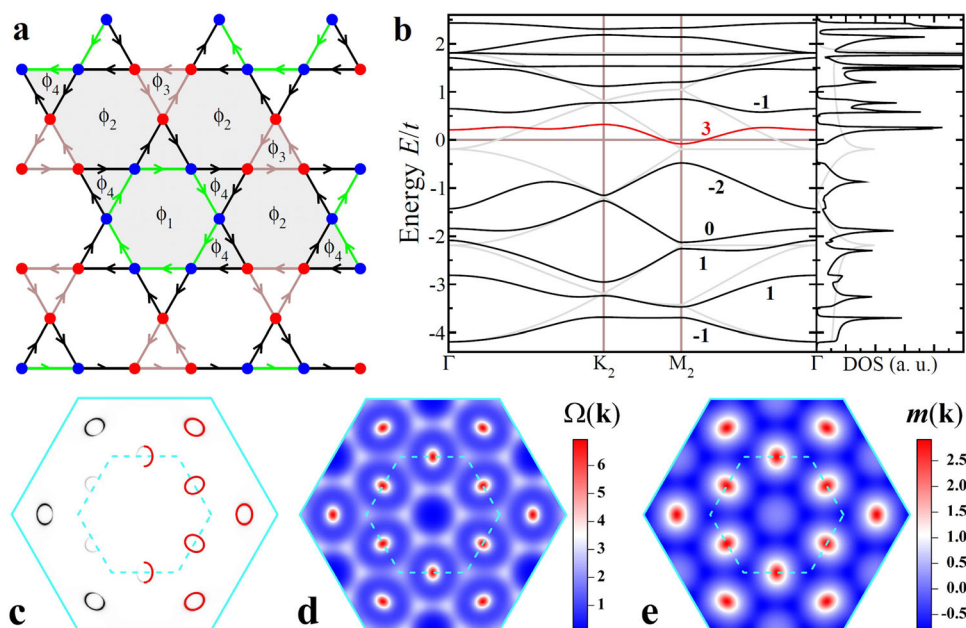


Fig. 2 | Complex CDW and Chern Fermi pockets. **a** Schematics of the $2a_0 \times 2a_0$ CDW state. Electron density is 0.878 (0.810) on the red (blue) sites. Three complex hoppings on the black, green, and brown bonds are $0.499 \pm 0.123i$, $0.345 \pm 0.162i$, and $0.349 \pm 0.110i$, respectively, giving rise to four independent plaquette fluxes $\phi_{1,\dots,4} = (0.840, -0.028, -0.291, 0.014)\pi$. The net flux through the unit cell (shaded grey) is zero. **b** Band dispersion in the folded BZ and DOS. Bands are marked by

corresponding Chern numbers. **c** Intensity plot of the DOS at the Fermi level, showing the spectral weight of the CFPs. Locations of the pockets are superimposed as red solid ellipses on the right half of the BZ. **d** Berry curvature distribution $\Omega(\mathbf{k})$ of the $C=3$ Chern band in **b**. **e** Orbital magnetic moment distribution $m(\mathbf{k})$ of the $C=3$ Chern band in unit of $ta_0^2 e/2\hbar$.

interactions can drive a complex CDW state⁴³ and produce an orbital Chern insulator^{37,44}. It has also been mentioned that finite doping or imperfect nesting may lead to secondary orders from the residual Fermi surfaces, such as the unidirectional charge order and the triple- \mathbf{Q} PDW⁴⁴. Since the actual Fermi level is away from the vH points of the d -bands at M in all three AV_3Sb_5 compounds^{16,28–32}, it is important to study the complex bond ordered phase close to but not at vH filling. As we show below, this results in a novel loop-current Chern metal with CFPs and an emergent primary PDW state detected in CsV_3Sb_5 ¹⁵.

We thus study the physics above vH filling ($n \geq n_{\text{vH}}$) by setting the symmetric hopping $t_{\alpha\beta}^+ = t$ uniform as the energy unit and the chemical potential $\mu = 0.19t$ in Eq. (2) with the sublattice resolved FS contour shown in Fig. 1d. The physics below vH filling is similar, with hole-like CFPs. The triple- \mathbf{Q} complex CDW described by H_{cdw} in Eq. (4) is generated by a complex ρ_v , which amounts to a correlation-induced breathing modulation of the antisymmetric hopping $t_{\alpha\beta}^- = \rho_v \cos(\mathbf{Q}_v^i \cdot \mathbf{r})$ in the single-orbital model in Eq. (2). Besides being physically intuitive, we find that such a complex CDW state with equal amplitudes in the $3\mathbf{Q}$ directions $\rho_v = \rho$ can be realized as the self-consistent mean field ground state driven by nn (V_1) and next-nn (V_2) Coulomb interactions (See Methods). Diagonalizing $H = H_{\text{ib}} + H_{\text{cdw}}$ with $\rho = (0.1 + 0.3i)(1, 1, 1)$, we obtain the $2a_0 \times 2a_0$ complex CDW state shown in Fig. 2a characterized by three different current-carrying bonds. Accumulating the link phases around the plaquettes produces four gauge-independent plaquette fluxes $\phi_{1,\dots,4}$ in the shaded 2×2 unit cell. The flux is staggered since the total flux $\Phi = \phi_1 + 3\phi_2 + 2\phi_3 + 6\phi_4$ is zero by symmetry. This orbital antiferromagnet breaks TRS but maintains inversion and C_6 rotation symmetry and gives rise to topological Chern bands on the kagome lattice.

The band dispersion and the DOS are shown in Fig. 2b in the reduced BZ. The Fermi level crosses the red Chern band with Chern number $C=3$ near the M_2 points, corresponding to electron doping of the Chern insulator at vH filling. The CDW metal is therefore a doped orbital Chern insulator with emergent CFPs, as shown in Fig. 2c, residing along Γ -K and around M_2 along Γ -M direction due to the 2×2 band folding (Fig. 1e). Each CFP has a volume -0.56% of

the original BZ. Remarkably, FS reconstruction and FS pockets of similar sizes have been detected by quantum oscillation experiments^{18,26,27}.

To understand the intriguing properties of the CFPs, we calculate the Berry curvature and orbital magnetic moment (See Methods) of the hosting $C=3$ Chern band. Figure 2d shows that the Berry curvature in momentum space $\Omega(\mathbf{k})$ concentrates heavily on the CFPs. Remarkably, small orbits carrying large Berry phase have indeed been detected in quantum oscillations^{18,26,27}. As a result, the CFPs contribute significantly to the AHE in addition to the fully occupied Chern bands in Fig. 2b: $\sigma_{xy} = 2 \frac{e^2}{h} - 2 \frac{e^2}{h} \int \frac{d^2k}{2\pi} \Omega(\mathbf{k}) \simeq 1.1 \frac{e^2}{h}$. Using the c -axis lattice constant $c \simeq 8.95 \text{ \AA}$, the magnitude of the intrinsic anomalous Hall conductivity is estimated $\sigma_{xy}/c \simeq 474 \Omega^{-1} \text{ cm}^{-1}$, which accounts for the observed large intrinsic AHE ($\sim 500 \Omega^{-1} \text{ cm}^{-1}$)^{23,24}. Moreover, the CFPs naturally lead to carrier density dependent intrinsic AHE observed by controlled gating in CsV_3Sb_5 nanoflakes⁴⁵.

The calculated orbital magnetic moment $m(\mathbf{k})$ is plotted in Fig. 2e for the $C=3$ Chern band hosting the CFPs in unit of $ta_0^2 e/2\hbar \simeq 1.9 \mu_B$ using the lattice constant $a_0 \simeq 5.4 \text{ \AA}$ and the hopping $t = 0.5 \text{ eV}$, corresponding to a 3 eV bandwidth of the d -band. The orbital moment, as large as $5 \mu_B$, concentrates on the CFPs and couples to an applied magnetic field along the c -axis via the orbital Zeeman effect $-m(\mathbf{k})B_z$. We thus expect strong and \mathbf{k} -dependent field-induced responses in the electronic structure. Moreover, the intrinsic thermodynamic orbital magnetization is calculated (Methods) to be $M \simeq -0.022 \mu_B$ per V, which is large enough to be detectable by thermodynamic measurements.

Vortex-antivortex lattice and roton PDW

The dynamically generated FS pockets are connected by well-defined momenta due to the band-folding. Figure 3a displays the 12 color coded CFPs. Pockets of the same color are related by the reciprocal lattice vectors of the $2a_0 \times 2a_0$ CDW $\mathbf{G}_{2a_0} = \frac{1}{2} \mathbf{G}$. Those of different colors are, in contrast, connected by new wave vectors $\mathbf{Q}_{4a_0} = \frac{1}{4} \mathbf{G}$ and $\mathbf{Q}_{3a_0} = \frac{3}{4} \mathbf{G}$ in all $3\mathbf{Q}$ directions, enabling new correlated quantum states that can coexist with the $2a_0 \times 2a_0$ CDW.

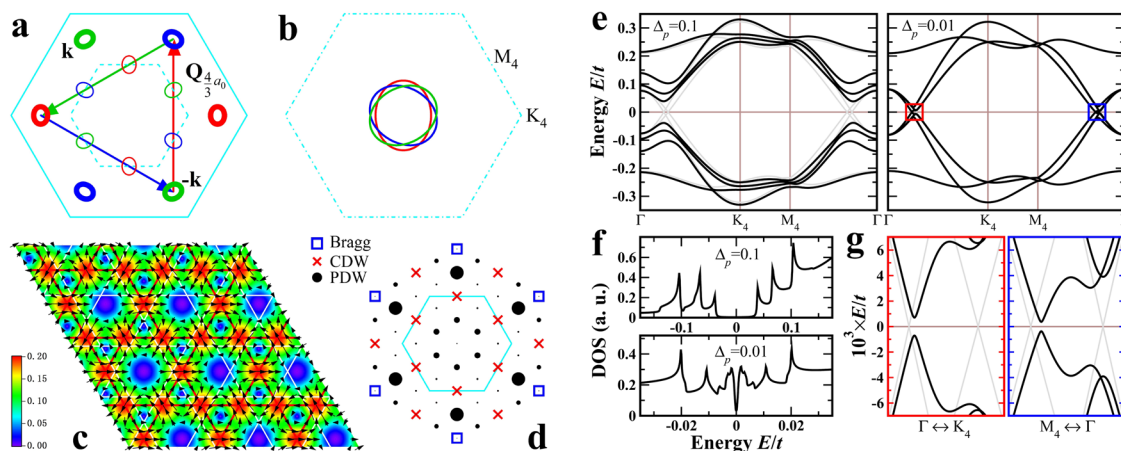


Fig. 3 | 3Q PDW and gapped CFPs. **a** Structure diagram of the CFPs. Pockets drawn in thick colored lines are connected by PDW wave vectors and carry most of the spectral weight (Fig. 2c). **b** Folded elliptical pockets in the 4×4 reduced BZ. **c** Spatial distribution of the $\frac{4}{3}a_0 \times \frac{4}{3}a_0$ complex PDW₁ order parameter for $\Delta_p = 0.1t$, with amplitude represented by color intensity and phase denoted by arrows. The emergent PDW kagomé lattice is shown by red lines, while the background kagomé lattice by white lines. Vortex and antivortex at the center of the triangles and hexagons are visible by the phase winding indicated by the arrowed black lines.

Note that neither \mathbf{Q}_{4a_0} nor $\mathbf{Q}_{\frac{4}{3}a_0}$ leads to full nesting because of the ellipticity of the pockets (Fig. 3b). Moreover, since the pockets are all electron-like, or all hole-like if the vH point is above the Fermi level, there is no instability in the particle-hole channel. Additional triple- \mathbf{Q} CDWs at these wave vectors cannot gap out the pockets (see Methods) and have not appeared experimentally, possibly because they are ineffective at lowering energy. A striped $4a_0$ charge order was however observed by STM on the Sb surface in CsV_3Sb_5 ^{13,15} which is allowed as a unidirectional single- \mathbf{Q} CDW in the Landau free energy analysis⁴⁶.

The path toward a stable correlated ground state can arise in the particle-particle channel through a PDW with finite momentum \mathbf{Q}_p pairing of a spin-down electron at momentum \mathbf{k} and a spin-up electron at $-\mathbf{k} + \mathbf{Q}_p$. In contrast to a CDW, it does not require the connected CFPs to be electron and hole like to produce a large susceptibility. The outer CFPs in Fig. 3a carry the majority of the spectral weight (Fig. 2c) and are more susceptible to a stabilizing PDW with $\frac{4}{3}a_0 \times \frac{4}{3}a_0$ periodicity (Methods). The energetically favorable triple- \mathbf{Q} PDW therefore has the wave vector $\mathbf{Q}_p = \mathbf{Q}_{\frac{4}{3}a_0} = \frac{3}{4}\mathbf{G}$, which connects each of the six outer elliptical pockets in Fig. 3a with its two neighbors. This corresponds precisely to the $\frac{4}{3}a_0 \times \frac{4}{3}a_0$ periodicity of the observed PDW₁¹⁵.

Pairing of electrons on the CFPs with orbital currents has not been studied previously. The staggered normal state loop-current must be confined to loop-supercurrent modulating the phase and circulating the vortices in the SC state, which is thus inhomogeneous with an emergent vortex-antivortex lattice. Since the microscopic pairing interaction is currently unknown, we consider the simplest onsite spin-singlet pairing,

$$H_{\text{pdw}} = - \sum_{\alpha\mathbf{r}} 2\Delta_{\text{pdw}}^{\alpha}(\mathbf{r})c_{\alpha\downarrow}^{\dagger}(\mathbf{r})c_{\alpha\uparrow}^{\dagger}(\mathbf{r}) + h.c., \quad (5)$$

where $\Delta_{\text{pdw}}^{\alpha}(\mathbf{r})$ is the order parameter on the α -sublattice in unit cell \mathbf{r} . Incommensurate hexagonal PDWs have been studied⁴⁷. For commensurate PDWs in the kagomé superconductors, a symmetry analysis taking into account the kagomé lattice and the intrinsic $2a_0 \times 2a_0$ CDW is necessary. The six basic PDW components carrying momenta $\pm \mathbf{Q}_p^{\eta}$ and centered at \mathbf{r}_0 can be written as

$$\Delta_{\pm \mathbf{Q}_p^{\eta}}(\mathbf{r}) = \Delta_p^{\pm \eta} e^{i\mathbf{Q}_p^{\eta} \cdot (\mathbf{r} - \mathbf{r}_0) \pm i\phi_{\eta}},$$

d Fourier peaks under coexisting $2a_0 \times 2a_0$ CDW and $\frac{4}{3}a_0 \times \frac{4}{3}a_0$ PDW₁. **e** Low-energy BdG quasiparticle bands in PDW₁ for $\Delta_p = 0.1t$ (left panel) and $0.01t$ (right panel) in the 4×4 folded BZ in **b**. Grey lines correspond to $\Delta_p = 0$. **f** Low-energy DOS of PDW₁. Top panel ($\Delta_p = 0.1t$) shows three pairs of coherence peaks at the PDW gaps of the three low-energy bands. Lower panel ($\Delta_p = 0.01t$) shows a V-shaped SC gap. A $k_B T = 10^{-4}t$ thermal broadening is applied. **g** Zoom-in of low-energy band dispersions inside red and blue boxes in the right panel of **e**, showing a full gap due to PDW induced uniform superconductivity.

where $\eta = 1, 2, 3$ denotes the three hexagonal directions and $2\phi_{\eta}$ is the relative phase between the $\pm \mathbf{Q}_p^{\eta}$ modes. Inversion and C_6 rotation symmetry requires that the amplitude and phase factor $\Delta_p^{\pm \eta} = \Delta_p e^{i\varphi_{\eta}}$, where $\varphi_{\eta} = \ell(\eta - 1)2\pi/3$ with $\ell = 0, \pm 1$ stems from the eigenvectors of rotation.

In contrast to the incommensurate case, the center \mathbf{r}_0 of the commensurate PDW must be pinned to equivalent C_6 rotation centers of the loop-current CDW in Fig. 2a (see Methods). A coherent superposition gives the allowed PDW states

$$\Delta_{\text{pdw}}^{\alpha}(\mathbf{r}) = e^{i\theta} \Delta_p \sum_{\eta=1,2,3} e^{i\varphi_{\eta}} \cos[\mathbf{Q}_p^{\eta} \cdot (\mathbf{r}_{\alpha} - \mathbf{r}_0) + \phi_{\eta}], \quad (6)$$

where θ is the global SC phase. Since there are 2×2 such \mathbf{r}_0 locations within each PDW unit cell that are connected by a π -phase shift, the symmetry of the PDW states described by Eq. (6) is $U(1) \times \mathbb{Z}_2 \times \mathbb{Z}_2$ and the phase ϕ_{η} can be defined as modulo π (see Methods). Among the possible PDWs, the complex PDWs with $\ell = \pm 1$ are consistent with the broken TRS of the loop-current CDW, and the states with $\phi_{\eta} = (0, 0, 0)$ are found to have a lower mean field energy, which will be denoted as PDW _{± 1} hereafter. The spatial distribution of the PDW₁ order parameter forms an emergent $\frac{4}{3}a_0 \times \frac{4}{3}a_0$ kagomé lattice as shown in Fig. 3c. The zeros of the order parameter located in the middle of the triangles and hexagons are the centers of the single-vortex and double-antivortex, respectively. Such a vortex-antivortex lattice, and thus the complex triple- \mathbf{Q} PDW _{± 1} , describes the conjectured roton-PDW₁¹⁵, based on the notion that a roton corresponds to a tightly bound vortex-antivortex pair.

Including the H_{pdw} , the total Bogoliubov-de Gennes (BdG) Hamiltonian can be diagonalized, giving rise to the Fourier peaks in the CDW and PDW field distributions in Fig. 3d. The BdG quasiparticle spectrum is shown in Fig. 3e. The PDW gap is expected to open first at the FS crossings⁴⁸ of the CFPs in Fig. 3b. For large enough PDW amplitudes, the CFPs are fully gapped, as shown in the left panel of Fig. 3e at $\Delta_p = 0.1t$. Three gapped quasiparticle bands, stemming from the three-colored CFPs, emerge with the minimum gap loci offset from the Fermi momenta. The corresponding low-energy DOS in Fig. 3f (top panel) reveals particle-hole symmetric gaps and three pairs of PDW peaks in remarkable agreement with the DOS spectrum observed in the SC state of CsV_3Sb_5 ¹⁵.

For weaker amplitude Δ_p , the PDW is expected to only gap out the crossings of the CFPs in Fig. 3b along Γ -K₄ and Γ -M₄ directions, leaving gapless excitations on the residual FS sections. Figure 3e (right panel) shows the quasiparticle dispersion of PDW₁ for an order of magnitude smaller $\Delta_p = 0.01t$. Surprisingly, the gapless PDW does not appear, and upon zooming in, a full excitation gap is still visible in Fig. 3g. Since the gap developed over the residual FS is small, the low energy DOS (Fig. 3f, bottom panel) shows a V-shaped SC gap inside the PDW gap at very low temperatures, with gap sizes ~0.7 meV and 10 meV for $t = 0.5eV$, in agreement with STM observations¹⁵. The fully gapped PDW state hints at an incipient uniform SC discussed below.

Intertwined CDW with orbital current

A primary PDW induces coexisting and intertwined electronic orders. The secondary order can become the primary vestigial order after the melting of the PDW by quantum and/or thermal fluctuations^{47–52}. We find that the hexagonal symmetry $\sum_{\eta} \mathbf{Q}_{\eta}^{\alpha} = 0$ and the intrinsic complex CDW lead to a plethora of novel intertwined and vestigial states. The induced CDWs originate from the bilinear products

$$\rho_{2\mathbf{Q}_p}^{\alpha}(\mathbf{r}) \propto \Delta_{\mathbf{Q}_p}^{\alpha}(\mathbf{r})\Delta_{-\mathbf{Q}_p}^{\alpha}(\mathbf{r}), \quad \rho_{\mathbf{Q}_p \pm \mathbf{Q}_p}^{\alpha}(\mathbf{r}) \propto \Delta_{\mathbf{Q}_p}^{\alpha}(\mathbf{r})\Delta_{\mp \mathbf{Q}_p}^{\alpha}(\mathbf{r}),$$

and carry wavevectors that coincide with those of the intrinsic CDW and primary PDW since $2\mathbf{Q}_p^{\alpha} = \mathbf{Q}_c^{\alpha} + \mathbf{G}^{\alpha}$, $\mathbf{Q}_p^{\alpha} + \mathbf{Q}_p^{\beta} = -\mathbf{Q}_p^{\gamma}$, and $\mathbf{Q}_p^{\alpha} - \mathbf{Q}_p^{\beta} = \mathbf{Q}_p^{\gamma} + \mathbf{G}_{2a_0}^{\alpha} + \mathbf{G}^{\alpha}$, where \mathbf{G} and \mathbf{G}_{2a_0} are the reciprocal vectors of the original and the 2×2 CDW lattice. Importantly, the complex PDW _{± 1} generates a complex triple- \mathbf{Q} CDW at \mathbf{Q}_p with nonzero angular momentum and orbital currents commensurate to those already present in the intrinsic loop-current CDW metal.

Fluctuating PDW and pseudogap phase

The PDW order parameter transforms under the phase change $\Delta_{\pm \mathbf{Q}_p}^{\alpha} \rightarrow e^{i\theta + i\varphi_{\eta} \pm i\Phi_{\eta}} \Delta_{\pm \mathbf{Q}_p}^{\alpha}$, where $\Phi_{\eta} = \mathbf{Q}_p^{\eta} \cdot \mathbf{u}$ are the phonon modes associated with the displacement field \mathbf{u} of the PDW vortex-antivortex lattice. For a commensurate density wave order, it is well known that coupling to electrons leads to collective phase modes with an energy gap $\propto \Delta_p(\Delta_p/W)^{(M-2)/2}$, where W is the bandwidth and M the commensurability ratio⁵³. Due to the $\mathbb{Z}_2 \times \mathbb{Z}_2$ commensurability locking, we have $M=2$, and the energy gap is on the order of the PDW gap, in contrast to the soft mode in the incommensurate case⁴⁷. This can be the reason for the robustness of the PDW observed in CsV₃Sb₅, having an energy gap around 5 mV¹⁵. When the proliferation of SC vortices in $\theta(\mathbf{r})$ due to quantum and/or thermal fluctuations drives $\langle \Delta_{\pm \mathbf{Q}_p}^{\alpha} \rangle = 0$, the induced CDWs $\rho_{\mathbf{Q}_p}^{\alpha}$, unaffected by the SC phase, become the vestigial ordered states detectable directly by STM at the intrinsic CDW and PDW wave vectors. The observed pseudogap phases¹⁵, both above T_c and in a strong magnetic field above H_{c2} , likely originate from such fluctuating PDW states.

Intertwined BCS instability

Intriguingly, the hexagonal symmetry allows a secondary uniform SC order⁴⁷,

$$\Delta_{2e}^{\alpha} \propto \Delta_{-\mathbf{Q}_p}^{\alpha}(\mathbf{r})\Delta_{\mathbf{Q}_p}^{\beta}(\mathbf{r})\Delta_{\mathbf{Q}_p}^{\gamma}(\mathbf{r}) = \Delta_p^3 e^{i(\theta - 2\varphi_{\alpha})}, \quad (7)$$

where $\sum_{\eta} \varphi_{\eta} = 2\pi$ was used. Accordingly, despite having only onsite pairing, a unique sublattice $d_{x^2-y^2} \pm id_{xy}$ superconductor with $\Delta_{2e}^{\pm} \propto \Delta_p^3(1, e^{\pm i2\pi/3}, e^{\mp i2\pi/3})$ arises and coexists with the primary roton PDW _{± 1} . The induced uniform charge-2e condensate ensures an intertwined BCS instability that fully gaps out the CFPs for arbitrarily small Δ_p as observed above.

Charge-4e and 6e superconductivity

The most striking intertwined and vestigial orders are the charge-4e and charge-6e superconductivity described by the spatially uniform

higher-charge SC order parameters

$$\Delta_{4e}^{\alpha} \propto \Delta_{\mathbf{Q}_p}^{\alpha}\Delta_{-\mathbf{Q}_p}^{\alpha} = \Delta_p^2 e^{i2(\theta + \varphi_{\alpha})}, \quad \Delta_{6e} \propto \Delta_{\mathbf{Q}_p}^{\alpha}\Delta_{\mathbf{Q}_p}^{\beta}\Delta_{\mathbf{Q}_p}^{\gamma} = \Delta_p^3 e^{i3\theta}. \quad (8)$$

Decoupled from the translational displacement field Φ_{η} of the PDW, they describe coexisting condensates of four-electron (two Cooper pairs) bound states in $d \pm id$ symmetry and six-electron (three Cooper pairs) bound states in isotropic s -wave symmetry, and raise the potential for realizing vestigial higher-charge superconductivity^{47,49,50,54,55}. Deep in the roton PDW state, the tightly bound vortex pairs form the hexagonal solid depicted in Fig. 3c. The vestigial order can thus be described by the celebrated Kosterlitz-Thouless-Halperin-Nelson-Young (KTHNY) theory for the staged melting of a vortex-antivortex lattice^{56–59}. In the KTHNY theory, the proliferation of topological defects, i.e., translational dislocations in Φ_{η} drives $\langle e^{i\Phi_{\alpha}} \rangle = 0$ and destroys the PDW order $\langle \Delta_{\pm \mathbf{Q}_p}^{\alpha} \rangle = 0$, as the vortex-antivortex lattice loses translation order and melts into a liquid crystal where the vestigial Δ_{2e} , Δ_{4e} , and Δ_{6e} prevail as the primary orders.

Note that, analogous to a nematic, this liquid crystal possesses discrete orientational order and is termed a hexatic⁵⁷. This can be seen in the $e^{\pm i2\varphi_{\alpha}}$ phase factors of Δ_{2e} and Δ_{4e} in Eq. (7) and Eq. (8). Thus this intermediate phase is a hexatic SC and the φ_{α} are related to the ordering directors. The hexatic order parameter is defined by $\Psi_6(\mathbf{r}) = e^{i6\varphi(\mathbf{r})}$, where $\varphi(\mathbf{r}) = \frac{1}{2}(\partial_x u_y - \partial_y u_x)$ measures the orientation of a neighboring vortex bond relative to a fixed axis under the displacement field⁵⁷. The hexatic SC is described by an effective low-energy Hamiltonian in the long-wavelength limit $\mathcal{H}/k_B T = \frac{\rho_s}{2}(\nabla\theta)^2 + \frac{K_A}{2}(\nabla\varphi)^2 - g_6 \cos(6\varphi)$ where ρ_s is the superfluid stiffness, K_A the Frank constant⁵⁷ for the hexatic stiffness, and g_6 the coupling constant for the six-fold anisotropy. The charge 2e, 4e and 6e fields exhibit power-law correlations $G_{2,4,6} \sim r^{-(\eta_s + 4\eta_A)}$, $r^{-4(\eta_s + \eta_A)}$, $r^{-9\eta_s}$ with $\eta_s = T/2\rho_s$ and $\eta_A = T/2\pi K_A$ in the hexatic vortex-antivortex phase.

The topological excitations in the hexatic SC can be revealed by the single-valuedness of the charge-2e order parameter Δ_{2e}^{α} in Eq. (7), i.e., along a path encircling a point defect $\oint d\theta - 2\oint d\varphi_{\alpha} = n_{\alpha} \times 2\pi$. The equations imply independent SC 2π -vortices in θ and 2π -disclinations in φ as well as π -single disclinations. Surprisingly, the solutions also support fractional $\frac{1}{3}$ -vortices⁴⁷ with a phase winding of $2\pi/3$ bound to $\frac{1}{3}$ -disclinations. The phase structure of such logarithmically interacting topological excitations is well-understood in the KTHNY theory by the vector Coulomb gases^{47,56–58}, which can be described by an effective sine-Gordon field theory $\mathcal{H}_{\text{dual}}$ for the dual fields of θ and φ ^{50,55}. In the region $K_A < \rho_s$, the hexatic undergoes a second stage melting with the proliferation of double disclinations into an isotropic liquid, where the correlation of $\Psi_6(\mathbf{r})$ decays exponentially and vortices are free. As a result, independent of the details of the transition, charge-2e and 4e condensates are destroyed by the exponential decay correlation of the $e^{\pm i2\varphi_{\alpha}}$ phase factors in the isotropic liquid, $\langle \Delta_{2e} \rangle = \langle \Delta_{4e} \rangle = 0$. Intriguingly, since the charge-6e order Δ_{6e} in Eq. (8) does not couple to φ and is unaffected by disclinations, its correlation remains algebraic. This is a novel SC phase with a charge-6e condensate and confined fractional $\frac{1}{3}$ -vortices. The transition from the charge-6e SC to the normal state proceeds by the unbinding and proliferation of fractional $1/3$ -vortices and $1/3$ -disclinations. While the detailed phase diagram deserves future studies, our findings suggest that the kagomé superconductors offer a promising platform for realizing higher-charge superconductivity.

Remarkably, charge-4e and charge-6e Little-Parks magnetoresistance oscillations have been observed very recently in mesoscopic ring structures fabricated using CsV₃Sb₅ flakes⁶⁰. It is conceivable that making the ring devices introduces significant lattice defects and strain fields that weakened and enabled the melting of the PDW before the SC phase coherence. Candidate charge-4e and charge-6e SC states are evidenced by the sequential change in the flux quantization from $hc/2e$

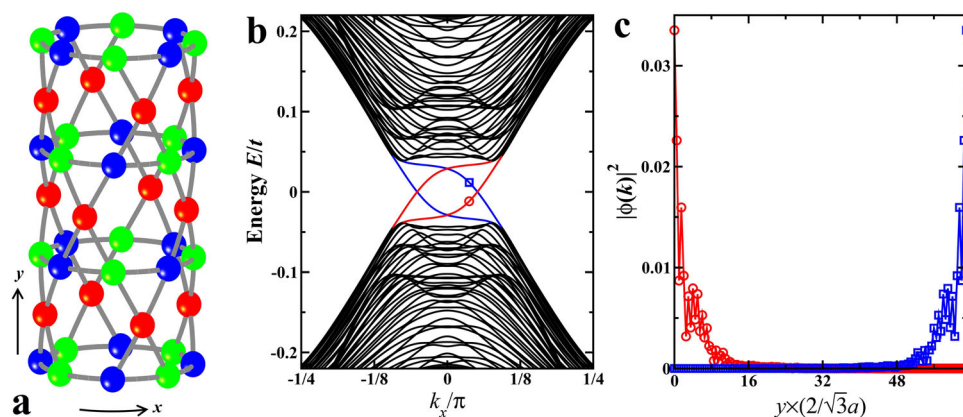


Fig. 4 | Chiral topological PDW and chiral edge modes. **a** Schematics of a cylindrical kagomé lattice with open boundaries in y -direction. A single 4×4 supercell is shown. Systems studied contain $L_x \times L_y$ supercells. An infinite L_x is used along the periodic direction in numerical calculations. **b** Low-energy quasiparticle spectrum of the triple-QPDW₁ at $\Delta_p = 0.1t$, showing two in-gap CEMs (blue

and red). $L_y = 64$ with 4×4 supercell. **c** Distribution along y -direction of the supercell averaged wavefunction amplitudes of the two in-gap CEMs indicated in **b** (red circle and blue square at $k_x = 3\pi/80$), showing localization at the opposite edges illustrated in **(a)**.

to $hc/4e$ and to robust $hc/6e$ over a widened fluctuation regime with increasing temperatures⁶⁰. Further theoretical and experimental studies are necessary to fully understand the possible realizations of higher-charge superconductivity.

Chiral topological PDW

The chiral PDW ground state with fully gapped CFPs carries an integer topological invariant $\mathcal{N} \in \mathbb{Z}$ given by the total Chern number of the occupied BdG quasiparticle bands in Fig. 3e. We obtain $\mathcal{N} = -2$ for PDW_{±L}, indicating two charge neutral chiral edge modes (CEMs) at the sample boundary. Under inversion symmetric open boundaries in y -direction (Fig. 4a), the spectrum of the BdG Hamiltonian for PDW₁ is plotted in Fig. 4b, as a function of the momentum k_x in the periodic x -direction. Two CEMs of equal chirality inside the SC gap (red and blue in Fig. 4b) pairwise localize on the opposite edges (Fig. 4c). We thus conclude that the triple-Q complex PDWs are intrinsic chiral topological superconductors.

Discussion

In this work, we studied loop-current Chern metals with CFPs and found several thought-provoking correlated and topological states of pertinent interests in quantum condensed matter physics. We proposed a novel mechanism for a class of PDW superconductors with loop-supercurrent circulating a vortex-antivortex lattice that emerge when the loop-current CDW metal enters the SC state. It offers a plausible explanation for the $\frac{4}{3}a_0 \times \frac{4}{3}a_0$ PDW observed in CsV₃Sb₅. The kagomé superconductors also exhibit fascinating phenomena associated with rotational symmetry breaking. The implications are discussed in Methods together with recent experimental findings. The microscopic origin of the pairing interaction in the multi-orbital AV₃Sb₅ is beyond the scope of this work. It can certainly be mediated by phonons and electron-phonon coupling¹⁶, given the weak local Coulomb repulsion and the absence of magnetism in AV₃Sb₅. In view of the orbital current and CFPs in the normal state, the pairing interaction can also be mediated by electronic fluctuations such as loop-current fluctuations^{48,61,62} and Pomeranchuk fluctuations of the reconstructed FSs in the CDW state⁶³. While a primary uniform charge-2e superconductor is unlikely to develop from the loop-current CDW, a complex roton PDW with a $2a_0 \times 2a_0$ vortex-antivortex lattice is not ruled out (“Methods”), which can be studied by microscopic model calculations in the future. In addition to the kagomé superconductors AV₃Sb₅, our findings are relevant for quantum materials exhibiting both orbital-driven anomalous Hall effect and superconductivity, such as the superconducting moiré graphene.

Methods

Realization of complex CDW in t - V_1 - V_2 model

The t - V_1 - V_2 model consists of nn hopping t , nn Coulomb repulsion V_1 , and next-nn Coulomb repulsion V_2 ,

$$H = -t \sum_{\langle i,j \rangle \sigma} (c_{i\sigma}^\dagger c_{j\sigma} + h.c.) + V_1 \sum_{\langle i,j \rangle} \hat{n}_i \hat{n}_j + V_2 \sum_{\langle\langle i,j \rangle\rangle} \hat{n}_i \hat{n}_j, \quad (9)$$

where $c_{i\sigma}^\dagger$ creates a spin- σ electron on site i , and the density operator $\hat{n}_i = \sum_{\sigma} c_{i\sigma}^\dagger c_{i\sigma}$. The Coulomb repulsions are decoupled in the density and bond channel by introducing $\hat{\chi}_{ij} = c_{i\uparrow}^\dagger c_{j\uparrow} + c_{i\downarrow}^\dagger c_{j\downarrow}$. The mean-field Hamiltonian is,

$$\begin{aligned} H_{\text{MF}} = & -t \sum_{\langle i,j \rangle \sigma} (c_{i\sigma}^\dagger c_{j\sigma} + h.c.) \\ & - V_1 \sum_{\langle i,j \rangle} (\chi_{ij}^* \hat{\chi}_{ij} + h.c. - |\chi_{ij}|^2 - 2n_i \hat{n}_j + n_i n_j) \\ & - V_2 \sum_{\langle\langle i,j \rangle\rangle} (\chi_{ij}^* \hat{\chi}_{ij} + h.c. - |\chi_{ij}|^2 - 2n_i \hat{n}_j + n_i n_j), \end{aligned} \quad (10)$$

where the density $n_i = \langle \hat{n}_i \rangle$ and the complex bond order parameters $\chi_{ij} = \langle \hat{\chi}_{ij} \rangle$ are determined fully self-consistently. We consider states that preserve C_6 rotation symmetry. The loop-current, when emerges, satisfies the continuity equation at the vertices of the kagomé lattice.

At vH filling, we obtain a $2a_0 \times 2a_0$ triple-Q complex CDW state, which is an orbital Chern insulator, driven by Coulomb repulsions $V_1 = 1.5t$ and $V_2 = 3t$. Increasing the band filling to $n = 5.064/12$, the self-consistently determined state is indeed a loop-current Chern metal with the band dispersion and the emergent CFPs shown in Fig. 5. The pattern of the loop-current on the nn bonds is identical to the one shown in Fig. 2a in the main text, with the complex hoppings on black, green, and brown bonds given by $0.487 \pm 0.071i$, $0.373 \pm 0.074i$, and $0.367 \pm 0.076i$, respectively. A detailed study of the t - V_1 - V_2 model is presented separately⁶⁴.

Berry curvature, anomalous Hall conductivity, orbital magnetic moment, and orbital magnetization

The Berry curvature of the n th quasiparticle band at momentum \mathbf{k} is given by⁶⁵

$$\begin{aligned} \Omega_n(\mathbf{k}) = & i \langle \nabla_{\mathbf{k}} u_{n\mathbf{k}} | \times | \nabla_{\mathbf{k}} u_{n\mathbf{k}} \rangle \\ = & i \left(\left\langle \frac{\partial u_{n\mathbf{k}}}{\partial k_x} \middle| \frac{\partial u_{n\mathbf{k}}}{\partial k_y} \right\rangle - \left\langle \frac{\partial u_{n\mathbf{k}}}{\partial k_y} \middle| \frac{\partial u_{n\mathbf{k}}}{\partial k_x} \right\rangle \right), \end{aligned} \quad (11)$$

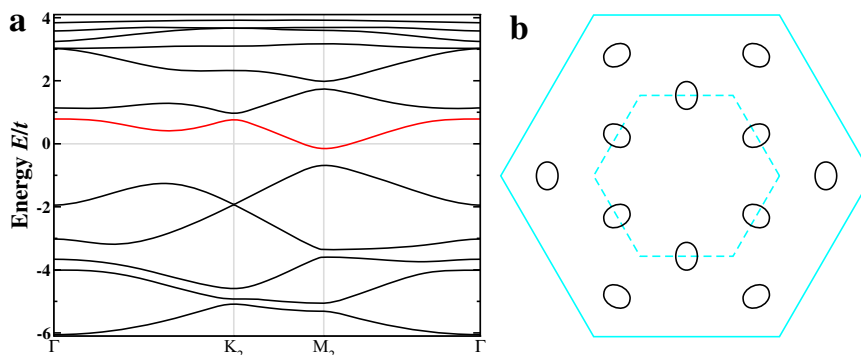


Fig. 5 | Complex CDW in t - V_1 - V_2 model. Band dispersion (a) in the 2×2 reduced BZ and the corresponding Chern FS pockets (b).

where $u_{n\mathbf{k}}$ is the periodic part of the Bloch state wave function. The Chern number of the corresponding band is obtained by integrating the Berry curvature over the BZ,

$$C_n = \int_{\text{BZ}} \frac{d\mathbf{k}}{2\pi} \Omega_n(\mathbf{k}). \quad (12)$$

The intrinsic contribution to the anomalous Hall conductivity in a 2D system is given by integrating the Berry curvature over all fully and partially occupied bands,

$$\sigma_{xy} = -\frac{e^2}{h} \sum_n \int_{\text{BZ}} \frac{d\mathbf{k}}{2\pi} \Omega_n(\mathbf{k}) f(\epsilon_{n\mathbf{k}}), \quad (13)$$

where $\epsilon_{n\mathbf{k}}$ is the energy dispersion of the n th band relative to the chemical potential, and f is the Fermi distribution function. The calculated intrinsic anomalous Hall conductivity in the main text contains contributions from both the fully occupied Chern bands and the CFPs in the doped orbital Chern insulator.

The Berry curvature also induces an orbital magnetic moment of the n th band at momentum \mathbf{k} ⁶⁵

$$\begin{aligned} \mathbf{m}_n(\mathbf{k}) &= -i \frac{e}{2\hbar} (\nabla_{\mathbf{k}} u_{n\mathbf{k}} \times (H_{\mathbf{k}} - \epsilon_{n\mathbf{k}}) \nabla_{\mathbf{k}} u_{n\mathbf{k}}) \\ &= -i \frac{e}{2\hbar} \left(\left(\frac{\partial u_{n\mathbf{k}}}{\partial k_x} (H_{\mathbf{k}} - \epsilon_{n\mathbf{k}}) \frac{\partial u_{n\mathbf{k}}}{\partial k_y} \right) - c.c. \right) \hat{z}, \end{aligned} \quad (14)$$

where $H_{\mathbf{k}}$ is the Hamiltonian of the system. Since the energy and wave vectors in this paper are measured in units of t and $1/a_0$, respectively, the obtained values of $\mathbf{m}(\mathbf{k})$ plotted in Fig. 2e is in units of $ta_0^2 e/2\hbar$. The orbital magnetic moment $\mathbf{m}(\mathbf{k})$ couples to an out-of-plane magnetic field by the orbital Zeeman effect and offers an intriguing pathway for field-tuning of the band structure. It is important to note that the orbital magnetic moment $\mathbf{m}(\mathbf{k})$ is different from the orbital magnetization \mathbf{M} that enters the thermodynamic potential $G = E - \mu N - \mathbf{M} \cdot \mathbf{B}$ and is given by

$$\mathbf{M} = \sum_n \int_{\text{BZ}} \frac{d\mathbf{k}}{(2\pi)^2} \left[\mathbf{m}_n(\mathbf{k}) - \frac{e}{\hbar} \epsilon_{n\mathbf{k}} \Omega_n(\mathbf{k}) \right] f(\epsilon_{n\mathbf{k}}). \quad (15)$$

It contains contributions from both the fully occupied Chern bands and the CFPs in the doped orbital Chern insulator away from van Hove filling, and can be measured in thermodynamic experiments.

$4a_0 \times 4a_0$ and $\frac{4}{3}a_0 \times \frac{4}{3}a_0$ CDW

The $2a_0 \times 2a_0$ CDW order causes FS reconstruction and the formation of the CFPs connected by the dynamically generated wave vectors \mathbf{Q}_{4a_0} or $\mathbf{Q}_{\frac{4}{3}a_0}$. Because the FS pockets are all electron-like, there is no instability in the particle-hole channel, making additional CDW

formation at these wave vectors unfavorable. To study their effect on the electronic structure, we consider additional $4a_0 \times 4a_0$ or $\frac{4}{3}a_0 \times \frac{4}{3}a_0$ CDWs in the simplest form,

$$\tilde{H}_{\text{cdw}} = \sum_{\alpha\sigma\mathbf{r}} \tilde{\rho}_{\alpha}(\mathbf{r}) c_{\alpha\sigma}^{\dagger}(\mathbf{r}) c_{\alpha\sigma}(\mathbf{r}), \quad (16)$$

with an onsite CDW potential

$$\tilde{\rho}_{\alpha}(\mathbf{r}) = \tilde{\rho} \sum_{\beta} \cos \left[\tilde{\mathbf{Q}}_{\text{cdw}}^{\beta} \cdot (\mathbf{r}_{\alpha} - \mathbf{r}_0) \right]. \quad (17)$$

Here, the ordering wave vectors $\tilde{\mathbf{Q}}_{\text{cdw}}$ is equal to \mathbf{Q}_{4a_0} or $\mathbf{Q}_{\frac{4}{3}a_0}$, and $\mathbf{r}_0 = (\frac{1}{4}, \frac{3\sqrt{3}}{4})$ is located at the C_6 /inversion center of the $2a_0 \times 2a_0$ CDW considered in the main text.

Diagonalizing $H_{\text{tb}} + H_{\text{cdw}} + \tilde{H}_{\text{cdw}}$, the resulting low-energy bands and FS are shown in Fig. 6 for a CDW potential $\tilde{\rho} = 0.1$ in the 4×4 folded BZ. The results in the absence of \tilde{H}_{cdw} are also plotted as brown curves for comparison. It can be seen clearly that neither $4a_0 \times 4a_0$ nor $\frac{4}{3}a_0 \times \frac{4}{3}a_0$ CDW can gap out the FS pockets. Instead, they reshape the pockets into different sizes centered around Γ in the 4×4 reduced BZ. As a result, the system cannot lower its energy significantly by forming such additional CDWs.

Commensurate PDW order on kagomé lattice

In the main text, the general form of the triple-Q PDW order parameter respecting the C_6 rotation and inversion symmetries has been derived and given in Eq. (6). We reproduced it here for the convince of discussion,

$$\Delta_{\text{pdw}}^{\alpha}(\mathbf{r}) = e^{i\theta} \sum_{\eta=1,2,3} e^{i\varphi_{\eta}} \Delta_p^{\eta} \cos \left[\mathbf{Q}_p^{\eta} \cdot (\mathbf{r}_{\alpha} - \mathbf{r}_0) + \phi_{\eta} \right], \quad (18)$$

where $\Delta_p^{\eta} = \Delta_p$, $\varphi_{\eta} = \ell(\eta-1)2\pi/3$ with $\ell = 0, \pm 1$, and \mathbf{r}_0 denotes the position of the commensurate PDW. In the presence of the underlying kagomé lattice and parent $2a_0 \times 2a_0$ loop-current CDW, \mathbf{r}_0 must locate at the center of the C_6 rotation and inversion of the CDW shown in Fig. 2a, and equivalent locations under $2a_0 \times 2a_0$ translations. Specifically, $\mathbf{r}_0 = (\frac{1}{4}, \frac{3\sqrt{3}}{4}) + 2n_1\mathbf{a}_1 + 2n_2\mathbf{a}_2$ with integers n_1 and n_2 . Additionally, the relative phase between $\pm \mathbf{Q}_p^{\eta}$ modes, ϕ_{η} , can only take the value of $(0, 0, 0)$ or $(\frac{\pi}{2}, \frac{\pi}{2}, \frac{\pi}{2})$ that changes the three cosine functions to sine functions.

Hereinafter, we refer to the PDW with $\phi_{\eta} = (0, 0, 0)$ as PDW_{ℓ} , and that with relative phase $(\frac{\pi}{2}, \frac{\pi}{2}, \frac{\pi}{2})$ as PDW'_{ℓ} . The spatial distributions of the pairing order parameters of the $\frac{4}{3}a_0 \times \frac{4}{3}a_0$ triple-Q PDWs are shown in Fig. 7 for PDW_0 (a), PDW'_1 (b), PDW'_0 (c), and PDW'_1 (d). PDW_0 and PDW'_0 are real and have circles of zeros and lines of zeros with maximum amplitudes forming triangular and honeycomb lattices,

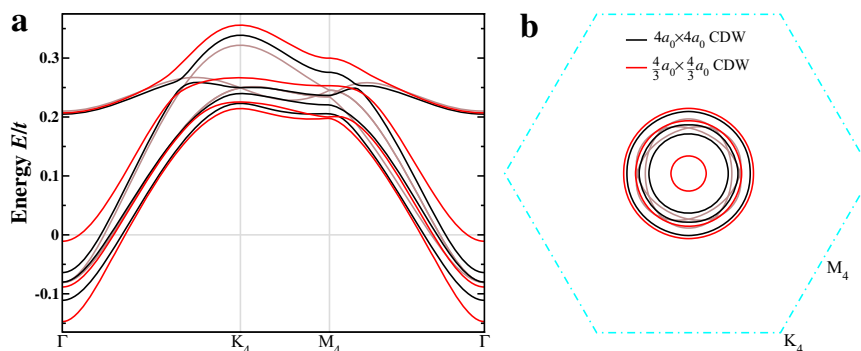


Fig. 6 | $4a_0 \times 4a_0$ and $\frac{4}{3}a_0 \times \frac{4}{3}a_0$ CDW. Low-energy bands (a) in the 4×4 reduced BZ and corresponding FS pockets (b) in the presence of additional $4a_0 \times 4a_0$ or $\frac{4}{3}a_0 \times \frac{4}{3}a_0$ CDW ($\rho = 0.1$). For comparison, band dispersion and FS pockets for the $2a_0 \times 2a_0$ CDW without additional electronic order correspond to the brown curves.

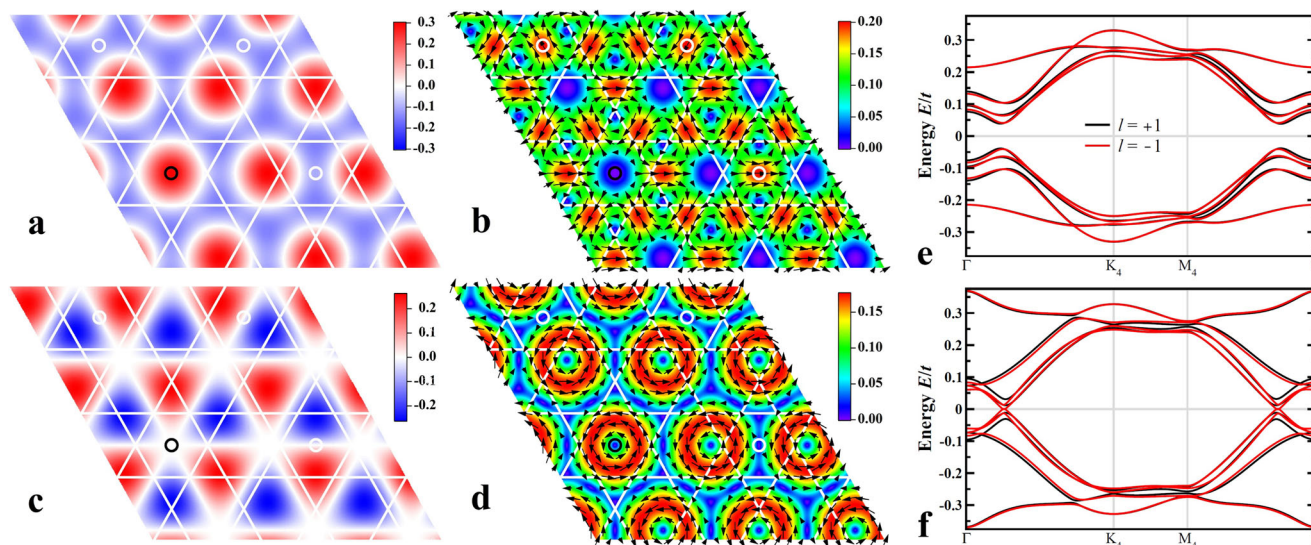


Fig. 7 | Commensurate $\frac{4}{3}a_0 \times \frac{4}{3}a_0$ PDWs. Spatial distribution of (a) PDW_0 , (b) PDW_1 , (c) PDW'_0 , and (d) PDW'_1 , evaluated with $\Delta_p = 0.1t$. Small black and white circles mark the C_6 rotation and inversion centers of the loop-current CDW in Fig. 2a. e Low-energy BdG quasiparticle bands for $\text{PDW}_{\pm 1}$. f Low-energy BdG

quasiparticle bands for $\text{PDW}'_{\pm 1}$. In (a) and (c), order parameters are real and represented by color intensity. In (b) and (d), order parameters are complex, with amplitude represented by color intensity and phase denoted by arrows.

respectively. The complex PDW_1 and PDW'_1 have point zeros forming emergent vortex-antivortex lattices.

The symmetry of the PDW states described by Eq. (18) is $U(1) \times \mathbb{Z}_2 \times \mathbb{Z}_2$, with $U(1)$ from the global SC phase. The discrete symmetries come from the 2×2 equivalent locations of \mathbf{r}_0 in each 4×4 PDW unit cell, which are marked by small black and white circles in Fig. 7a-d. Under a translation $\mathbf{r}_0 \rightarrow \mathbf{r}_0 + 2\mathbf{a}_{1,2}$, since $2\mathbf{Q}_p^\eta \cdot \mathbf{a}_{\eta'} = 3\pi(1 - \delta_{\eta\eta'})$, the PDW components in Eq. (18) gain a π -phase shift in the cosine functions in two of the three hexagonal directions, while the remaining one is unaltered. The $\mathbb{Z}_2 \times \mathbb{Z}_2$ symmetry arises because the transformed state can be brought back to the original one by a combination of $4a_0 \times 4a_0$ translation and inversion symmetry operations. Equivalently, this symmetry can be understood as the BdG quasiparticle dispersions of the PDW being invariant under $\Delta_p^\eta \rightarrow -\Delta_p^\eta$ in Eq. (18). As a result, the relative phase φ_η in Eq. (18) and Eq. (6) in the main text can be defined as modulo π .

Because the parent loop-current Chern metal breaks TRS, only the complex triple-Q PDW states with $\ell = \pm 1$ need to be considered further. Including the H_{pdw} for the complex chiral PDW with $\ell = \pm 1$, the total BdG Hamiltonian can be diagonalized, giving rise to the quasiparticle spectrum shown in Fig. 7e and 7f. Clearly, compared to $\text{PDW}_{\pm 1}$, $\text{PDW}'_{\pm 1}$ of the same amplitude are much less effective at gapping out the

quasiparticle bands and thus expected to be energetically unfavorable. Calculating the mean-field state energies, defined as the expectation of the total BdG Hamiltonian $E_{\text{PDW}} = \langle H_{\text{tb}} + H_{\text{cdw}} + H_{\text{pdw}} \rangle$, we find that $\text{PDW}'_{\pm 1}$ have substantially higher energy than that of $\text{PDW}_{\pm 1}$, while the energy of PDW_1 is lower than that of PDW_{-1} for the chosen normal state loop-current direction on the bonds. Accordingly, we focused our study on PDW_1 in the main text.

Finally, we make connections to the incommensurate hexagonal PDW first studied in ref. 47 in the effective continuum limit. Without considering the underlying lattice and the parent commensurate CDW, the center of the PDW, \mathbf{r}_0 , can slide freely along the three hexagonal directions. This leads to two independent continuous and undetermined phases, $\phi'_1 = \mathbf{Q}_p^1 \cdot \mathbf{r}_0$ and $\phi'_2 = \mathbf{Q}_p^2 \cdot \mathbf{r}_0$, and a $\phi'_3 = \mathbf{Q}_p^3 \cdot \mathbf{r}_0 = -\phi'_1 - \phi'_2$, corresponding to the two Goldstone modes of the PDW states having $U(1) \times U(1) \times U(1)$ symmetry as discussed in ref. 47. In this case, PDW_0 , $\text{PDW}_{\pm 1}$, PDW'_0 , and $\text{PDW}'_{\pm 1}$ recover Ψ_Δ , Ψ_{kag} , Ψ_{hc} , and $\Psi_{\text{hc},2}$ in Table I of ref. 47, correspondingly.

$4a_0 \times 4a_0$ and $2a_0 \times 2a_0$ PDW

Figure 8 shows the low-energy BdG quasiparticle bands for the $4a_0 \times 4a_0$ and $2a_0 \times 2a_0$ $\text{PDW}_{\pm 1}$ states in the 4×4 reduced BZ. Compared to those shown in Fig. 3e in the main text for the

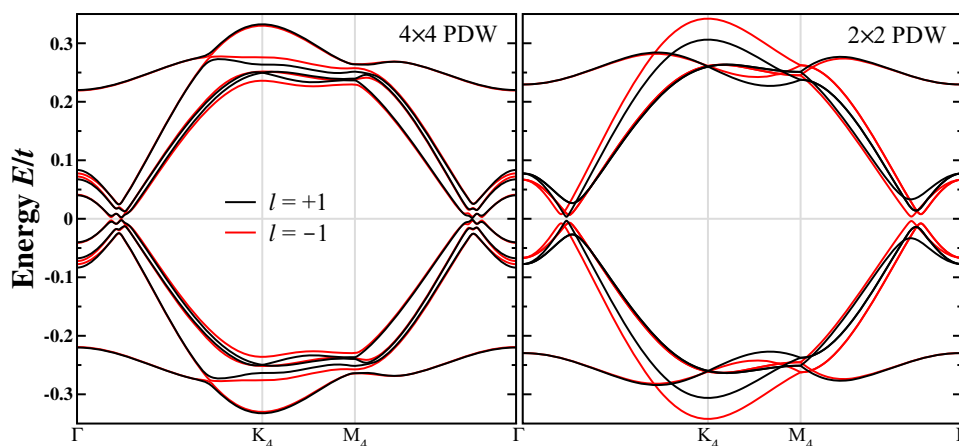


Fig. 8 | $4a_0 \times 4a_0$ and $2a_0 \times 2a_0$ PDW. Low-energy BdG quasiparticle bands for the 3Q PDW $_{\pm 1}$ states with $\Delta_p = 0.1t$ along high-symmetry path in the 4×4 reduced BZ.

The bands of the $2a_0 \times 2a_0$ PDW are folded into the 4×4 reduced BZ for the convenience of comparison.

$\frac{4}{3}a_0 \times \frac{4}{3}a_0$ PDW that pairs electrons on the outer FS pockets carrying the majority of the spectral weight (Fig. 3a), the $4a_0 \times 4a_0$ and $2a_0 \times 2a_0$ PDW of the same amplitude are much less effective at gapping out the quasiparticle bands and thus not the energetically favorable PDW states. This does not rule out the possible coexistence of these primary PDW states, which are all capable of producing a smaller full gap due to the induced secondary uniform superconductivity.

Rotation and reflection symmetry breaking

In the original STM study of KV₃Sb₅, the intensity of the six CDW peaks in the Fourier transform of the conductance map breaks *all* reflection symmetries and thus exhibits a handedness, which can be flipped by a magnetic field¹². The existence of this chiral CDW is currently debated. A later STM work¹⁹ finds that the handedness is absent, while a *single* reflection symmetry about one of the hexagonal directions, i.e. a reflection axis, remains and supports a rotational symmetry breaking CDW with 120° oriented C₂ domains. Moreover, the rotation symmetry is generally broken at high temperatures near the CDW transition⁶⁶, independent of the $4a_0$ charge stripe order that appears around 50–60K in CsV₃Sb₅¹³, but not in KV₃Sb₅^{12,19}. However, the coherent electronic state with two-fold symmetry emerges only at low temperatures as indicated by the unidirectional quasiparticle interference patterns visible below about 35K⁶⁶, which is consistent with the two-fold electronic state observed in NMR and elastoresistance measurements⁶⁷. These findings suggest that the rotation symmetry breaking down to C₂ at T_{cdw} can be driven by the out of phase stacking of the in-plane $2a_0 \times 2a_0$ CDW with alternating SD and inverse-SD lattice distortions^{16,43,68,69}.

Most recently, all three 120° oriented C₂ domains have been observed to onset at T_{cdw} by optical birefringence scanning probes in all three kagome metals AV₃Sb₅⁷⁰. In each of the C₂ domains, TRS breaking is detected by optical Kerr rotation and circular dichroism⁷⁰, which can be described by the complex CDW in Eq. (4) with the real part of hopping in ρ_y along the reflection axis different from the other two directions. The complex nonchiral phase factors⁴⁴ in ρ_y produce a similar loop-current distribution. Correspondingly, the triple-Q PDW can break the rotation symmetry with the amplitude Δ_p^n in Eq. (18) taking a different value along the reflection axis. Thus we expect the results discussed here to be applicable to AV₃Sb₅ under weak rotation symmetry breaking.

Data availability

The data that support the findings of this study are available from the corresponding authors upon request.

Code availability

The code that support the findings of this study are available from the corresponding authors upon request.

References

- Ortiz, B. R. et al. New kagome prototype materials: discovery of KV₃Sb₅, RbV₃Sb₅, and CsV₃Sb₅. *Phys. Rev. Mater.* **3**, 094407 (2019).
- Ortiz, B. R. et al. CsV₃Sb₅: A Z₂ topological kagome metal with a superconducting ground state. *Phys. Rev. Lett.* **125**, 247002 (2020).
- Han, T.-H. et al. Fractionalized excitations in the spin-liquid state of a kagome lattice antiferromagnet. *Nature* **492**, 406 (2012).
- Norman, M. R. Herbertsmithite and the search for the quantum spin liquid. *Rev. Mod. Phys.* **88**, 041002 (2016).
- Ko, W.-H., Lee, P. A. & Wen, X.-G. Doped kagome system as exotic superconductor. *Phys. Rev. B* **79**, 214502 (2009).
- Ye, L. et al. Massive Dirac fermions in a ferromagnetic kagome metal. *Nature* **555**, 638 (2018).
- Yin, J.-X. et al. Giant and anisotropic many-body spin-orbit tunability in a strongly correlated kagome magnet. *Nature* **562**, 91 (2018).
- Liu, D. F. et al. Magnetic Weyl semimetal phase in a kagomé crystal. *Science* **365**, 1282 (2019).
- Morali, N. et al. Fermi-arc diversity on surface terminations of the magnetic Weyl semimetal Co₃Sn₂S₂. *Science* **365**, 1286 (2019).
- Liu, E. et al. Giant anomalous Hall effect in a ferromagnetic kagome-lattice semimetal. *Nat. Phys.* **14**, 1125 (2018).
- Yin, J.-X. et al. Negative flat band magnetism in a spin-orbit-coupled correlated kagome magnet. *Nat. Phys.* **15**, 443 (2019).
- Jiang, Y.-X. et al. Unconventional chiral charge order in kagome superconductor KV₃Sb₅. *Nat. Mater.* **20**, 1353 (2021).
- Zhao, H. et al. Cascade of correlated electron states in a kagome superconductor CsV₃Sb₅. *Nature* **599**, 216 (2021).
- Liang, Z. et al. Three-dimensional charge density wave and surface-dependent vortex-core states in a kagome superconductor CsV₃Sb₅. *Phys. Rev. X* **11**, 031026 (2021).
- Chen, H. et al. Roton pair density wave in a strong-coupling kagome superconductor. *Nature* **599**, 222 (2021).
- Tan, H., Liu, Y., Wang, Z. & Yan, B. Charge density waves and electronic properties of superconducting kagome metals. *Phys. Rev. Lett.* **127**, 046401 (2021).
- Li, H. et al. Observation of unconventional charge density wave without acoustic phonon anomaly in kagome superconductors AV₃Sb₅ (A=Rb, Cs). *Phys. Rev. X* **11**, 031050 (2021).
- Ortiz, B. R. et al. Fermi surface mapping and the nature of charge density wave order in the kagome superconductor CsV₃Sb₅. *Phys. Rev. X* **11**, 041030 (2021).

19. Li, H. et al. Rotation symmetry breaking in the normal state of a kagome superconductor KV_3Sb_5 . *Nat. Phys.* **18**, 265 (2022).
20. Mielke III, C. et al. Time-reversal symmetry-breaking charge order in a correlated kagome superconductor. *Nature* **602**, 245 (2022).
21. Yu, L. et al. Evidence of a hidden flux phase in the topological kagome metal CsV_3Sb_5 . Preprint at <https://arxiv.org/abs/2107.10714> (2021).
22. Wu, Q. et al. Simultaneous formation of two-fold rotation symmetry with charge order in the kagome superconductor CsV_3Sb_5 by optical polarization rotation measurement. *Phys. Rev. B* **106**, 205109 (2022).
23. Yang, S.-Y. et al. Giant, unconventional anomalous Hall effect in the metallic frustrated magnet candidate, KV_3Sb_5 . *Sci. Adv.* **6**, eabb6003 (2020).
24. Yu, F. H. et al. Concurrence of anomalous Hall effect and charge density wave in a superconducting topological kagome metal. *Phys. Rev. B* **104**, L041103 (2021).
25. Xiang, Y. et al. Twofold symmetry of c-axis resistivity in topological kagome superconductor CsV_3Sb_5 with in-plane rotating magnetic field. *Nat. Commun.* **12**, 6727 (2021).
26. Fu, Y. et al. Quantum transport evidence of topological band structures of kagome superconductor CsV_3Sb_5 . *Phys. Rev. Lett.* **127**, 207002 (2021).
27. Shrestha, K. et al. Nontrivial Fermi surface topology of the kagome superconductor CsV_3Sb_5 probed by de Haas-van Alphen oscillations. *Phys. Rev. B* **105**, 024508 (2022).
28. Wang, Z. et al. Distinctive momentum dependent charge-density-wave gap observed in CsV_3Sb_5 superconductor with topological Kagome lattice. Preprint at <https://arxiv.org/abs/2104.05556> (2021).
29. Nakayama, K. et al. Multiple energy scales and anisotropic energy gap in the charge-density-wave phase of kagome superconductor CsV_3Sb_5 . *Phys. Rev. B* **104**, L161112 (2021).
30. Hu, Y. et al. Charge-order-assisted topological surface states and flat bands in the kagome superconductor CsV_3Sb_5 . *Science Bulletin* **67**, 495 (2022).
31. Kang, M. et al. Twofold van Hove singularity and origin of charge order in topological kagome superconductor CsV_3Sb_5 . *Nat. Phys.* **18**, 301 (2022).
32. Luo, H. et al. Electronic nature of charge density wave and electron-phonon coupling in kagome superconductor KV_3Sb_5 . *Nat. Commun.* **13**, 273 (2022).
33. Bolens, A. & Nagaosa, N. Topological states on the breathing kagome lattice. *Phys. Rev. B* **99**, 165141 (2019).
34. Kiesel, M. L. & Thomale, R. Sublattice interference in the kagome Hubbard model. *Phys. Rev. B* **86**, 121105R (2012).
35. Wang, W. S., Li, Z. Z., Xiang, Y. Y. & Wang, Q.-H. Competing electronic orders on kagome lattices at van Hove filling. *Phys. Rev. B* **87**, 115135 (2013).
36. Kiesel, M. L., Platt, C. & Thomale, R. Unconventional fermi surface instabilities in the Kagome Hubbard model. *Phys. Rev. Lett.* **110**, 126405 (2013).
37. Hsu, T. C., Marston, J. B. & Affleck, I. Two observable features of the staggered-flux phase at nonzero doping. *Phys. Rev. B* **43**, 2866 (1991).
38. Chakravarty, S., Laughlin, R. B., Morr, D. K. & Nayak, C. Hidden order in the cuprates. *Phys. Rev. B* **63**, 094503 (2001).
39. Varma, C. M. Theory of the pseudogap state of the cuprates. *Phys. Rev. B* **73**, 155113 (2006).
40. Haldane, F. D. M. Model for a quantum Hall effect without Landau levels: condensed-matter realization of the parity anomaly. *Phys. Rev. Lett.* **61**, 2015 (1988).
41. Fang, X., Jiang, K., Wang, Z. & Hu, J. Chiral flux phase in the kagome superconductor AV_3Sb_5 . *Science Bulletin* **66**, 1384 (2021).
42. Denner, M. M., Thomale, R. & Neupert, T. Analysis of charge order in the kagome metal AV_3Sb_5 (A=K, Rb, Cs). *Phys. Rev. Lett.* **127**, 217601 (2021).
43. Park, T., Ye, M. & Balents, L. Electronic instabilities of kagome metals: saddle points and Landau theory. *Phys. Rev. B* **104**, 035142 (2021).
44. Lin, Y.-P. & Nandkishore, R. M. Complex charge density waves at Van Hove singularity on hexagonal lattices: Haldane-model phase diagram and potential realization in kagome metals AV_3Sb_5 (A=K, Rb, Cs). *Phys. Rev. B* **104**, 045122 (2021).
45. Zheng, G. et al. Electrically controlled superconductor-insulator transition and giant anomalous Hall effect in kagome metal CsV_3Sb_5 nanoflakes. Preprint at <https://arxiv.org/abs/2109.12588> (2021).
46. McMillan, W. L. Landau theory of charge-density waves in transition-metal dichalcogenides. *Phys. Rev. B* **12**, 1187 (1975).
47. Agterberg, D. F., Geracie, M. & Tsunetsugu, H. Conventional and charge-six superfluids from melting hexagonal Fulde-Ferrell-Larkin-Ovchinnikov phases in two dimensions. *Phys. Rev. B* **84**, 014513 (2011).
48. Lee, P. A. Amperean pairing and the pseudogap phase of cuprate superconductors. *Phys. Rev. X* **4**, 031017 (2014).
49. Agterberg, D. F. & Tsunetsugu, H. Dislocations and vortices in pair-density-wave superconductors. *Nat. Phys.* **4**, 639 (2008).
50. Berg, E., Fradkin, E. & Kivelson, S. A. Charge-4e superconductivity from pair-density-wave order in certain high-temperature superconductors. *Nat. Phys.* **5**, 830 (2009).
51. Dai, Z., Zhang, Y.-H., Senthil, T. & Lee, P. A. Pair-density waves, charge-density waves, and vortices in high- T_c cuprates. *Phys. Rev. B* **97**, 174511 (2018).
52. Agterberg, D. F. et al. The physics of pair-density waves: cuprate superconductors and beyond. *Annu. Rev. Condens. Matter Phys.* **11**, 231 (2020).
53. Lee, P. A., Rice, T. M. & Anderson, P. W. Conductivity from charge or spin density waves. *Solid State Commun.* **14**, 703 (1974).
54. Fernandes, R. M. & Fu, L. Charge-4e superconductivity from multi-component nematic pairing: Application to twisted bilayer graphene. *Phys. Rev. Lett.* **127**, 047001 (2021).
55. Jian, S.-K., Huang, Y. & Yao, H. Charge-4e superconductivity from nematic superconductors in two and three Dimensions. *Phys. Rev. Lett.* **127**, 227001 (2021).
56. Kosterlitz, J. M. & Thouless, D. J. Ordering, metastability and phase transitions in two-dimensional systems. *J. Phys. C* **6**, 1181 (1973).
57. Nelson, D. R. & Halperin, B. I. Dislocation-mediated melting in two dimensions. *Phys. Rev. B* **19**, 2457 (1979).
58. Young, A. P. Melting and the vector Coulomb gas in two dimensions. *Phys. Rev. B* **19**, 1855 (1979).
59. Chaikin, P. M. & Lubensky, T. C. Principles of condensed matter physics, Cambridge University Press, (1995).
60. Ge, J. et al. Discovery of charge-4e and charge-6e superconductivity in kagome superconductor CsV_3Sb_5 . Preprint at <https://arxiv.org/abs/2201.10352> (2022).
61. Wang, Z., Kotliar, G. & Wang, X.-F. Flux-density wave and superconducting instability of the staggered-flux phase. *Phys. Rev. B* **42**, 8690(R) (1990).
62. Aji, V., Shekhter, A. & Varma, C. M. Theory of the coupling of quantum-critical fluctuations to fermions and d-wave superconductivity in cuprates. *Phys. Rev. B* **81**, 064515 (2010).
63. Lin, Y.-P. & Nandkishore, R. M. Multidome superconductivity in charge density wave kagome metals. *Phys. Rev. B* **106**, L060507 (2022).

64. Dong, J.-W., Wang, Z. & Zhou, S. Loop-current charge density wave driven by long-range Coulomb repulsion on the kagomé lattice. Preprint at <https://arxiv.org/abs/2209.10768> (2022).
65. Xiao, D., Chang, M. C. & Niu, Q. Berry phase effects on electronic properties. *Rev. Mod. Phys.* **82**, 1959 (2010).
66. Li, H. et al. Emergence of unidirectional coherent quasiparticles from high-temperature rotational symmetry broken phase of AV_3Sb_5 kagome superconductors. Preprint at <https://arxiv.org/abs/2203.15057> (2022).
67. Nie, L. et al. Charge-density-wave-driven electronic nematicity in a kagome superconductor. *Nature* **604**, 59 (2022).
68. Christensen, M. H., Birol, T., Andersen, B. M. & Fernandes, R. M. Theory of the charge density wave in AV_3Sb_5 kagome metals. *Phys. Rev. B* **104**, 214513 (2021).
69. Maio, H. et al. Geometry of the charge density wave in the kagome metal AV_3Sb_5 . *Phys. Rev. B* **104**, 195132 (2021).
70. Xu, Y. et al. Three-state nematicity and magneto-optical Kerr effect in the charge density waves in kagome superconductors. *Nat. Phys.* <https://doi.org/10.1038/s41567-022-01805-7> (2022).

Acknowledgements

We thank Binghai Yan, Kun Jiang, Jiangping Hu, Keyu Zeng, Jiaxin Yin, Zahid Hasan, He Zhao, Ilija Zeljkovic, Hu Miao, Stephen Wilson, and especially Hui Chen and Hongjun Gao for valuable discussions. S.Z. is supported by the National Key R&D Program of China (Grant No. 2022YFA1403800), the Strategic Priority Research Program of CAS (Grant No. XDB28000000), and the National Natural Science Foundation of China (Grants No. 11974362 and No. 12047503). Z.W. is supported by the U.S. Department of Energy, Basic Energy Sciences (Grant No. DE-FG02-99ER45747) and by the Cottrell SEED Award No. 27856 from Research Corporation for Science Advancement. Numerical calculations were performed on the HPC Cluster of ITP-CAS. Z.W. thanks Aspen Center for Physics for hospitality and acknowledges the support of NSF Grant No. PHY-1607611.

Author contributions

S.Z. and Z.W. contributed to all aspects of this work and wrote the paper.

Competing interests

The authors declare no competing interests.

Additional information

Correspondence and requests for materials should be addressed to Sen Zhou or Ziqiang Wang.

Peer review information *Nature Communications* thanks the anonymous reviewer(s) for their contribution to the peer review of this work.

Reprints and permissions information is available at <http://www.nature.com/reprints>

Publisher's note Springer Nature remains neutral with regard to jurisdictional claims in published maps and institutional affiliations.

Open Access This article is licensed under a Creative Commons Attribution 4.0 International License, which permits use, sharing, adaptation, distribution and reproduction in any medium or format, as long as you give appropriate credit to the original author(s) and the source, provide a link to the Creative Commons license, and indicate if changes were made. The images or other third party material in this article are included in the article's Creative Commons license, unless indicated otherwise in a credit line to the material. If material is not included in the article's Creative Commons license and your intended use is not permitted by statutory regulation or exceeds the permitted use, you will need to obtain permission directly from the copyright holder. To view a copy of this license, visit <http://creativecommons.org/licenses/by/4.0/>.

© The Author(s) 2022